Science of the Total Environment 1006 (2025) 180909

Contents lists available at ScienceDirect

Science of the Total Environment

journal homepage: www.elsevier.com/locate/scitotenv

Factors contributing to elevated springtime surface ozone levels in eastern China

Fanghe Zhao [a], Yuhang Wang [a,*], Lewis Gregory Huey [a], Shengjun Xi [a], Young Ro Lee [a], Wei Song [b], Xinming Wang [b], Jianhui Tang [c], Kezhen Chong [a], Hang Qu [a]

[a] School of Earth and Atmospheric Sciences, Georgia Institute of Technology, Atlanta, GA, USA
[b] State Key Laboratory of Organic Geochemistry, Guangzhou Institute of Geochemistry, Chinese Academy of Sciences, Guangzhou, China
[c] CAS Key Laboratory of Coastal Environmental Processes and Ecological Remediation, Yantai Institute of Coastal Zone Research, Chinese Academy of Sciences, Yantai, China

HIGHLIGHTS

- Spring ozone in NCP exceeded California by 50 % and the eastern U.S. by 85 % in 2018.
- Reactive Aromatics drive 73 % of ozone production; model underestimates by up to 22 %.
- Redistributing emissions and adding diurnal cycles greatly improve simulated ozone.
- Emission redistribution shifts NCP from VOC-limited to more NO_x-limited, reversing NO_x sensitivity.
- Misallocated aromatics emissions raise ozone mortality by ~50,000 deaths/year.

GRAPHICAL ABSTRACT

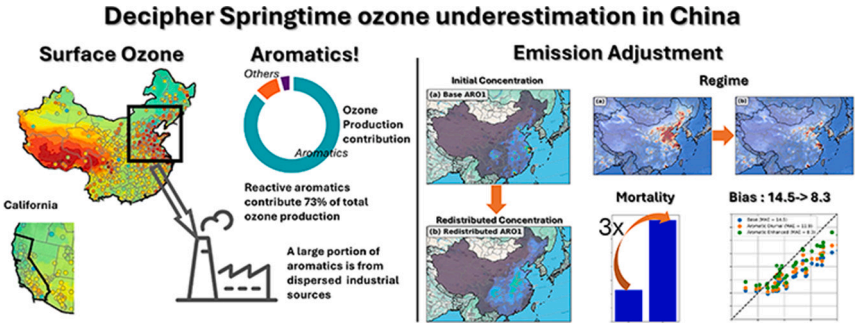

ARTICLE INFO

Keywords:
North China Plain
Springtime ozone
Aromatics emissions
Ozone production regimes
Industrial emissions

ABSTRACT

Springtime ozone levels in the North China Plain (NCP) exceed those in California by 50 %. The difference is even larger at 85 % when compared to the eastern U.S. Field measurements at a rural NCP site reveal reactive aromatics concentrations 6.2 times higher than California levels, respectively. Box model analysis demonstrates reactive aromatics contribute 73 % of the total ozone production. By redistributing reactive aromatics emissions based on industrial source patterns and implementing observation-constrained diurnal cycles, model performance improves significantly across the NCP region. This redistribution shifts the chemical regime from predominantly VOC-limited into a transition zone towards NO_x-limited regime, reversing the effect of NO_x reduction on ozone in the NCP region. The underestimation of reactive aromatics emissions has substantial public health implications through increased ozone-related mortality. Our findings underscore the critical need for improved characterization of industrial emissions in economically developing regions to enable effective air quality management strategies.

* Corresponding author.
E-mail address: yuhang.wang@eas.gatech.edu (Y. Wang).

https://doi.org/10.1016/j.scitotenv.2025.180909
Received 6 August 2025; Received in revised form 22 October 2025; Accepted 5 November 2025

1. Introduction

Tropospheric ozone is a major secondary pollutant that poses significant risks to health and vegetation, and acts as a short-lived climate forcer (Bell et al., 2006; Cohen et al., 2017; Li et al., 2017; Liu et al., 2018; Punger and West, 2013; Tanaka, 2015; Yue and Unger, 2014; Zhang et al., 2019). China is facing severe ozone pollution, with concentrations in both urban and remote regions frequently exceeding regulatory standards (Fu et al., 2019; Li et al., 2020a; Lu et al., 2018; Xue et al., 2014). Compared to polluted U.S. regions such as California (Demetillo et al., 2019; Huang et al., 2013; Jin et al., 2008), the North China Plain (NCP) exhibits approximately 50 % higher springtime (March and April) ozone levels based on maximum daily 8-h average (MDA8). Previous studies have documented this seasonal challenge, with Ni et al. (2018) highlighting springtime ozone pollution issues particularly in the NCP region. Wang et al. (2022) reported elevated ozone concentrations in the NCP during spring, daily average ozone reaching 134.83 μg/m^3 from 2016 to 2020.

Tropospheric ozone forms through photochemistry of nitrogen oxides (NOx) and volatile organic compounds (VOCs) (Seinfeld and Pandis, 2016). The ozone formation potential varies significantly among VOC species. Because of their high OH reactivity and radical production potential, reactive aromatics (e.g. xylenes) and small alkenes ($<C_5$) are often more effective in driving ozone formation than alkanes (Zheng and Xie, 2025). Aromatics have been identified as significant ozone precursors in China, accounting for approximately 37 % of ozone formation potential in Beijing (Li et al., 2020b). Previous research indicates that the NCP region is typically in VOC-limited or transitional regimes during winter and summer (Li et al., 2021b; Liu et al., 2012b; Lyu et al., 2019; Yang et al., 2021). However, springtime ozone production remain insufficiently characterized, where current atmospheric models tend to underestimate springtime ozone concentrations in the NCP, in part due to inaccurate anthropogenic emission inventories (Li et al., 2021b; Ni et al., 2018) and background ozone (Li et al., 2021a). In particular, multiple studies have identified significant underestimations of aromatics emissions in China. Liu et al. (2012a) found that aromatics emissions were underestimated by factors of 4–10 through top-down inversions using glyoxal column measurements, while Li et al. (2017) reported a threefold underestimation based on secondary organic aerosol concentrations during autumn.

The complex emission source characteristics further complicate ozone production in the NCP region. Provinces like Shandong and Hebei are home to over 6000 and 4000 heavy industrial plants, respectively (Wang et al., 2022). These facilities create complex patterns of ozone precursor distributions that may not be accurately represented in current emission inventories. Recent work by Oliveira et al. (2024) highlighted the significant contribution of industrial solvent sectors to toluene and xylene emissions, while Wang et al. (2020) observed pronounced diurnal cycles in aromatics emissions in Shanghai. Despite these findings, understanding the impact of spatiotemporal variability in aromatic emissions on springtime ozone production remains limited, particularly in the NCP region.

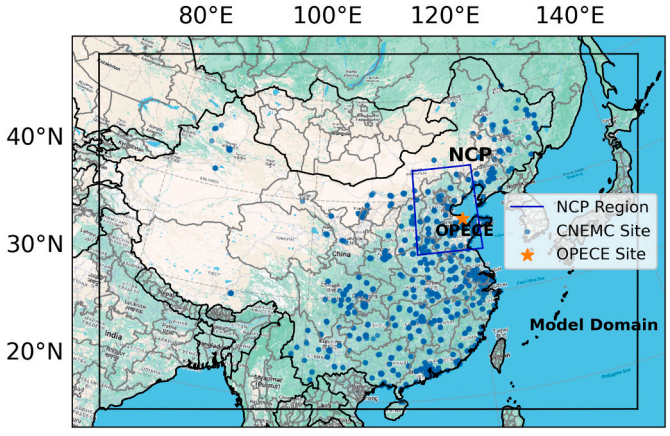

Fig. 1. Model domain and observation network configuration for North China Plain ozone study. Map of East Asia showing the regional model domain (black box) and the North China Plain region (blue box). The OPECE Dongying measurement site is marked by an orange star, and blue dots indicate the locations of CNEMC (China National Environmental Monitoring Centre) observation sites across eastern China.

To address this, we investigated the role of aromatics emissions in springtime ozone pollution across the NCP using a multi-scale model approach that integrates 3-D Chemical Transport Model (CTM) and 0-D box model simulations with observations from the Ozone Photochemistry and Export in Coastal Environment (OPECE) campaign. We estimated the contribution of different VOC species to ozone production using box model simulations incorporating a near-explicit chemical mechanism. We then evaluated two major model enhancements: redistributing aromatic emissions spatially based on observed industrial source patterns and incorporating observation-based diurnal emission cycles. These modifications substantially improved model's accuracy in predicting springtime ozone concentrations. The resulting shifts in ozone production regimes across the region have significant implications for developing effective ozone control strategies in this rapidly industrializing region.

2. Materials and methods

2.1. Ground observation

We utilized the observations from the OPECE campaign (Chong et al., 2024a, 2024b; Lee et al., 2021), conducted at a rural coastal site (37.76°N, 118.98°E) in the Yellow River Delta region near the Shandong Yellow River Delta National Nature Reserve from March 23 to April 22, 2018. The remote measurement location, approximately 50 km northeast of Dongying city and downwind from the NCP region, allowed us to assess regional transport and photochemical processing of air pollutants. Comprehensive in situ measurements during OPECE include trace gases (O_3, NO_2, NO, HNO_2, CO, SO_2) and non-methane volatile organic compounds (NMVOCs), at minute and hourly data resolutions, respectively, along with meteorological variables and photolysis rates (Lee et al., 2021).

To extend our analysis beyond a single site and evaluate regional pollutant distributions, we incorporated data from the China National Environmental Monitoring Center (CNEMC) network. This extensive monitoring infrastructure, established since 2013, provided hourly measurements of six criteria pollutants (O_3, CO, NO_2, SO_2, $PM_{2.5}$, PM_{10}) from 1320 sites nationwide (China National Environmental Monitoring Center Network, 2018; Kong et al., 2021). We applied rigorous data filtering protocols following Qu et al. (2020) to eliminate measurement outliers, ensuring high data quality for our regional analysis during March–April 2018.

2.2. Regional atmospheric chemistry transport model

We used a multi-scale modeling approach combining three-dimensional (3-D) and zero-dimensional (0-D) simulations to evaluate photochemical processes. The Regional chEmical and trAnsport Model (REAM) served as our primary modeling framework due to its proven capability in simulating East Asian atmospheric chemistry (Chong et al., 2024b; Li et al., 2019; Li et al., 2021a; Liu et al., 2012b; Qu et al., 2020; Qu et al., 2021; Yan et al., 2021). For the 3-D simulations, we configured REAM with a 36 km × 36 km horizontal resolution across China with 30 vertical layers, balancing computational efficiency with the ability to resolve regional pollution patterns. We incorporated meteorological fields from the Weather Research and Forecasting (WRF-ARW v4) model using Four-Dimensional Data Assimilation (FDDA) constrained by the

ECMWF Reanalysis v5 (ERA5) dataset (Hersbach et al., 2020), capturing synoptic conditions during the study period. Chemical boundary conditions were derived from monthly averages of the ECMWF Atmospheric Composition Reanalysis 4 (EAC4) (Inness et al., 2019), which represented background conditions for long-lived species. The model was initialized with a 10-day spin-up period to establish realistic chemical conditions and minimize the influence of initial values on our analysis period.

The chemical mechanism extends the GEOS-Chem framework with aromatics reactions from SAPRC-07 (Carter, 2010), to capture the ozone production from aromatics oxidation products (Yan et al., 2019). We based all anthropogenic emissions on the Multiresolution Emission Inventory for China (MEIC) (Cheng et al., 2023; Cheng et al., 2021; Tong et al., 2020) with a monthly resolution, including NOx, NMVOCs, CO, and other pollutants participating in atmospheric chemical reactions, and incorporating NO_x weekday-to-weekend emission ratios and emission diurnal profiles following Li et al. (2021b). The spatial distributions of all emission inventories are shown in Fig. S1. Biogenic emissions were dynamically calculated using the Model of Emissions of Gases and Aerosols from Nature (MEGAN v2.1) (Guenther et al., 2012). The observation site location and model domain are shown in Fig. 1.

To enable direct comparison and validate model performance, we conducted parallel CONUS domain simulations using identical model physics and chemical mechanisms. This comparative modeling approach allowed us to evaluate regional differences in ozone simulation performance and identify potential biases in the Chinese domain results (detailed US domain configuration in Text S1).

Measured VOCs were aggregated into lumped species categories following the GEOS-Chem chemical mechanism naming convention. Explicit species include ethene (C_2H_4), ethane (C_2H_6), propane (C_3H_8), benzene (BEN), and isoprene (ISOP). Lumped categories include alkenes (PRPE), saturated aliphatics (ALK4), and two reactive aromatics groups differentiated by OH reactivity: ARO1 (OH rate constants $<1 \times 10^{-11}$ cm^3 $molecule^{-1}$ s^{-1}) and ARO2 (OH rate constants $>1 \times 10^{-11}$ cm^3 $molecule^{-1}$ s^{-1}). Details about species classifications are provided in Text S2.

For the 0-D box model simulations, we employed two chemical mechanisms: the same mechanism used in the 3-D model for consistency, and the more detailed Master Chemical Mechanism (MCM v3.3.1) (Jenkin et al., 2003; Jenkin et al., 2015) for comprehensive analysis. These simulations enabled us to simulate radical concentrations, quantify radical budgets, and evaluate ozone production rates (detailed methodology in Text S3).

To quantify ozone production rates, we applied the formulation from Qu et al. (2020) and Hao et al. (2024):

$$P_{O_3} = k_{HO_2+NO} * [HO_2] * [NO] + \sum_i k_{RO_2^i+NO} * [RO_2^i] * [NO] \quad (1)$$

where k_{HO_2+NO} is the chemistry reaction constant of HO_2 reacting with NO, and $k_{RO_2^i+NO}$ is the chemistry reaction constant of each of the RO_2 species reacting with NO.

To characterize the photochemical regime, we performed sensitivity simulations with 50 % NO_x emission reductions (Li et al., 2013) and analyzed the resulting changes in O_3 concentrations. Additionally, we developed a regime indicator based on the Ln/Q approach (Kleinman, 2005; Mazzuca et al., 2016), defined as the ratio between primary radical loss rate due to the reaction of OH + NO_2 and the total radical production rate from photolysis of H_2O_2 and oxygenated VOCs (OVOCs):

$$I_{Regime} = \frac{Rate_{NO_2+OH\rightarrow HNO3}}{Rate_{OVOC+h\nu\rightarrow HO_2} + Rate_{OVOC+h\nu\rightarrow RO_2} + Rate_{O_3+h\nu\rightarrow O_{1d}} + 2*Rate_{H_2O_2+h\nu\rightarrow HO_2}} \quad (2)$$

Values of I_{Regime} approaching 1 indicate that radical loss is predominantly associated with the reaction of OH + NO_2, signifying a VOC-limited regime, whereas I_{Regime} values approaching 0 suggest a NO_x-limited regime.

Table 1
Summary of simulation experiments with different emission configurations.

Case	Description
C_0	Base case using monthly MEIC emissions with standard NOx diurnal cycle
C_1	Base case with observation-constrained aromatics diurnal cycle
C_2	C_1 with redistributed aromatics emissions based on industrial source patterns
C_0–50 % NOx	Base case with a 50 % reduction in NOx emissions
C_2–50 % NOx	C_2 with a 50 % reduction in NOx emissions

To estimate the contributions of individual VOCs to ozone production, we assess how ozone production rates change upon the removal of selected VOCs in model simulations (i.e., zero-out sensitivity analysis) (Liaskoni et al., 2024; Qu et al., 2021; Zhang et al., 2020). This method involved comparing ozone concentrations between a baseline simulation (including all VOCs) and simulations where specific VOCs were sequentially removed from the model. The difference in ozone concentrations between the full model and each sensitivity model represents the ozone production contributions attributable to the eliminated VOC species (Qu et al., 2021):

$$\Delta P_{O_3}^{VOC_i} = P_{O_3}^{Base} - P_{O_3}^{Zero\ VOC_i} \quad (3)$$

The MCM mechanism explicitly represents all cross-reactions, radical recycling, and synergistic effects among precursor groups, enabling comprehensive assessment of VOC interactions in ozone formation. Zero-out sensitivity analysis (Eq. 3) captures both direct and indirect effects of individual VOC contributions within this chemical framework.

2.3. VOCs source apportionment and aromatics emission diagnosis

We applied the Positive Matrix Factorization (PMF) model v5.0 (Brown et al., 2015) to field measurements to differentiate VOC emissions into five distinct source categories, following configurations established by Cai et al. (2010). This analysis revealed that aromatic compounds primarily originated from industrial rather than urban sources, providing critical information for redistributing emissions, which significantly reduced the bias in simulated ozone.

We also improved the diurnal emission profile of aromatics using the mass-balance approach methodology described by Wang et al. (2020). This approach calculates the emission rate by considering concentration changes, chemical loss, and transport processes according to the following equation:

$$E_{aromatics} = \frac{\partial[ARO]}{\partial t} + k_{ARO+OH} * [ARO] * [OH] + T \quad (4)$$

where $E_{aromatics}$ represents the emission rate of aromatics, $\frac{\partial[ARO]}{\partial t}$ denotes the rate of change in aromatics concentration, $k_{ARO+OH} * [ARO] * [OH]$ denote the chemical reaction rate for hydroxyl oxidation of aromatics, and T accounts for the net transport flux for advection. The transport calculation uses the background concentration flux to determine the net emission rate into or out of the observation site. We used a background concentration of reactive aromatics of 2.0 ppbv according to Zhang et al. (2016), Wu and Xie (2017) and Zhang et al. (2025). The ARO1 and ARO2 speciation is based on OPECE in situ measurements.

To investigate the impact of the diurnal profile and spatial distribution of aromatics emissions on ozone concentrations, we conducted four simulation experiments with varying emission configurations (Table 1). The base case (C0) employed monthly MEIC emissions with NOx diurnal cycles from Li et al. (2021c). Case 1 (C1) implemented observation-constrained aromatics diurnal emission profile derived from OPECE measurements. Case 2 (C2) built upon C1 by redistributing

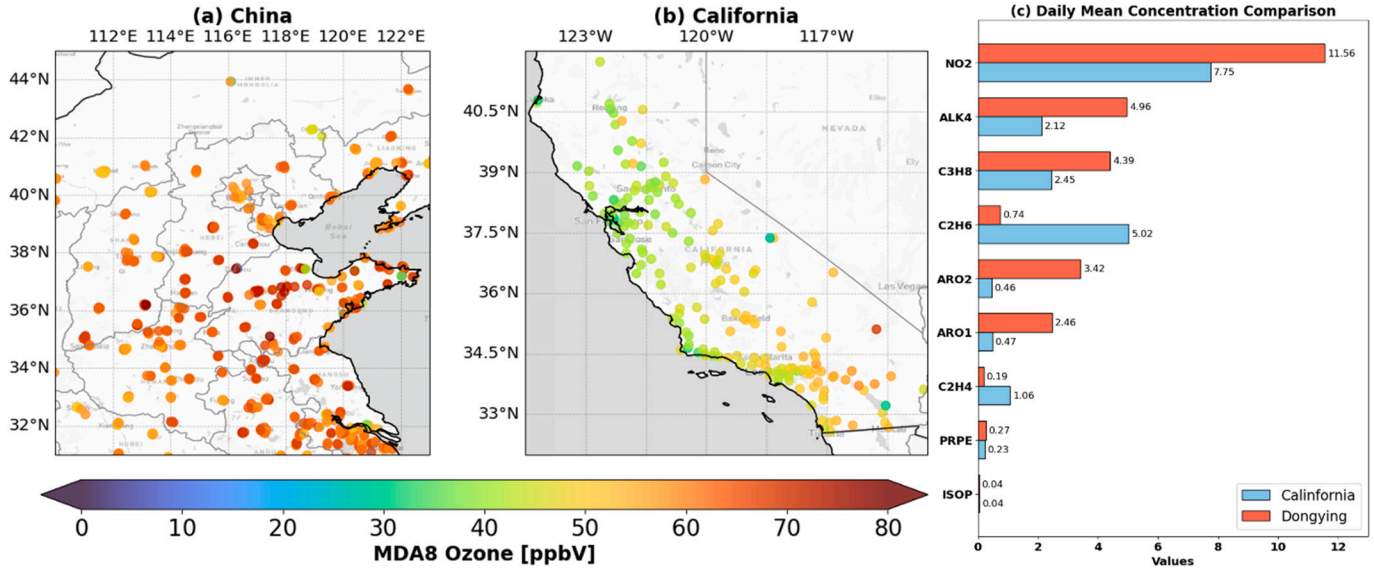

Fig. 2. Elevated ozone concentrations in the NCP region and much higher reactive aromatics at the OPECE site compared to California. (a) Spatial distribution of maximum daily 8-h average (MDA8) ozone concentrations across the North China Plain for March and April 2018. (b) Corresponding MDA8 ozone distribution across California for the same period, using identical color scaling for direct comparison. (c) Comparison of daily mean concentrations for key atmospheric species between California (blue bars) and the OPECE site (red bars), showing the concentration ratios for VOCs and NO_2. PRPE denotes ≥C3 alkenes, ALK4 denotes ≥C4 alkanes, and ISOP denotes isoprene.

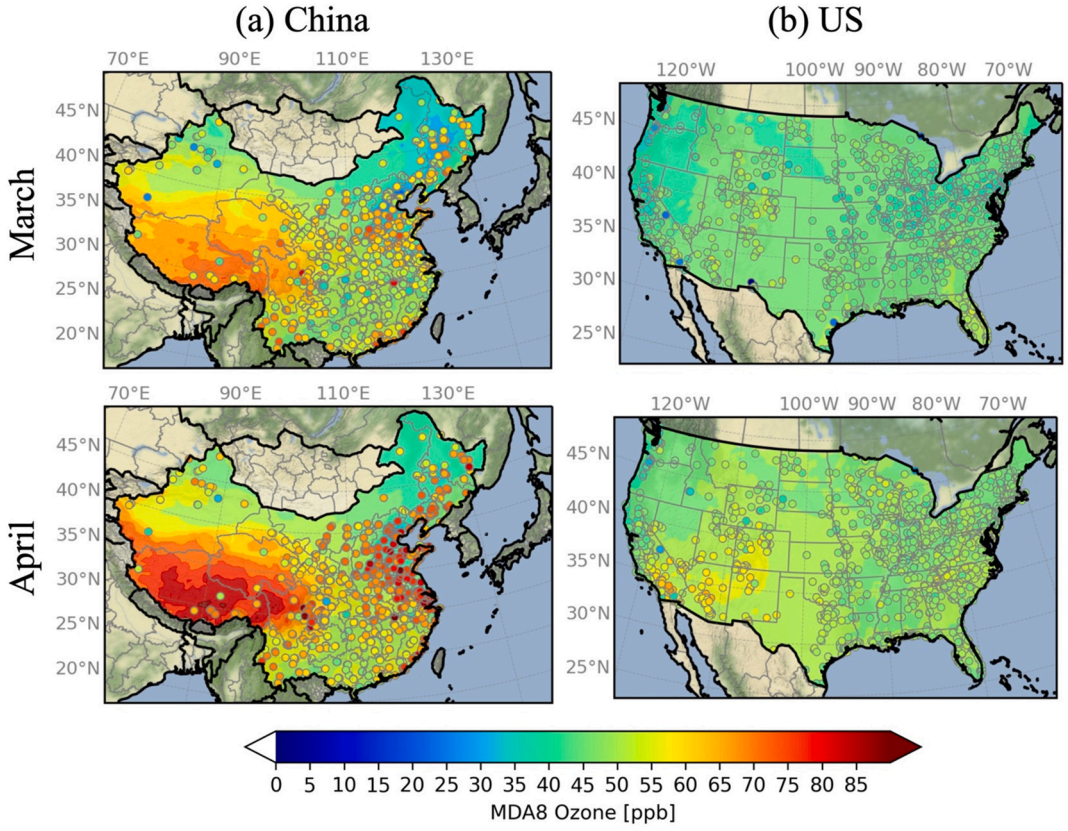

Fig. 3. Model simulated maximum daily 8-h average ozone concentrations for March and April 2018: (a) China and (b) United States. Observed concentrations are shown by color-coded circles.

aromatics emissions based on OVOC industrial emission patterns identified through PMF analysis, which indicated that aromatics primarily originate from industrial sources rather than urban centers. This redistribution dispersed aromatics emissions more broadly across the NCP region compared to the original MEIC inventory. To assess ozone sensitivity to NOx reductions, we conducted additional simulations (C0–50 %NOx and C2–50 %NOx) with 50 % reduced NOx emissions for the base (C0) and redistributed aromatic emission (C2) cases, enabling

evaluation of chemical regime transitions resulting from redistributed aromatics emissions.

3. Results

3.1. Higher springtime ozone in NCP than California and eastern U.S. and model simulation disparity

The NCP region exhibits substantially higher springtime ozone concentrations compared to California in March and April 2018. Maximum daily 8-h average (MDA8) ozone values in the NCP region exceed those in California by 50 % on average (Fig. 2a–b). Among O_3 precursors, averaged concentrations of reactive aromatics (e.g., ARO1 and ARO2) at the OPECE site were 5–7 times higher than those in California, while NO_2 concentrations show only a modest 1.4-times increase (Fig. 1c). Model simulations in this work suggest that elevated aromatic levels in the NCP contribute to the marked MDA8 ozone differences between the NCP and California, as aromatic oxidation strongly modulates photochemical ozone production pathways (e.g., Liu et al. (2012b) and Liu et al. (2012a)).

The observed springtime ozone mixing ratios across the U.S., including elevated levels in southern California, are reasonably explained by model simulations (Fig. 3). The gradual increase of springtime ozone over the United States was analyzed extensively using surface, aircraft, and satellite observations (Choi et al., 2008; Wang et al., 2003). Despite a different meteorological year and considerably higher NOx emissions than 2018, an earlier version of REAM reproduced the observed surface ozone increase from February to May in 2000. The observed and simulated ozone increase from March to April in the U.S. (Choi et al., 2008) are comparable to 2018 (Fig. 3). The gradual springtime ozone increase over North America largely corresponds to the increases in primary HO_x ($OH + HO_2$) sources and partition of NOx towards NO as solar radiation increases (Wang et al., 2003).

In contrast, simulated ozone concentrations are 10–40 ppbV lower than the observations over the NCP region (Fig. 3b). The underestimation reaches the ozone level over the northeastern U.S. in March, suggesting fundamental gaps in our understanding of springtime ozone formation in regions with significant precursor emissions from complex sources. To diagnose the chemical mechanisms responsible for this systematic underestimation, we examined the contributions of individual VOC species to ozone production using model simulations with detailed chemical mechanisms implemented in both REAM and MCM.

The contrasting model performance between eastern China and the U.S. using identical modeling framework and boundary condition source demonstrates that the NCP ozone underestimation reflects region-specific emission deficiencies rather than systematic model structural biases. This comparative analysis effectively controls potential confounding factors, including background ozone, vertical exchange processes, and fundamental model physics, which would similarly affect the simulations for some regions of the U.S. if they were the primary bias sources. Additionally, the similarity of observed and simulated surface ozone increases from March to April in 2000 (Choi et al., 2008) and 2018 (Fig. 3) over the United States, a vast polluted region at northern midlatitudes as eastern China, further strengthens this argument. The EAC4 global reanalysis also simulated similar ozone concentrations (Fig. S2), indicating that the substantial modeling biases over the NCP region, absent in the U.S., are not model-specific. In fact, the global simulation shows similar ozone concentrations over the polluted low-elevation regions in China, U.S., and Europe during March–April 2018.

We quantitatively evaluated model performance using multiple statistical metrics including correlation coefficient (R), mean absolute error (MAE), and root mean squared error (RMSE). Table S2 presents comprehensive statistical validation for ozone and reactive aromatics at the OPECE site across different emission scenarios. These metrics demonstrate substantial improvement in ozone simulation accuracy following aromatics emission redistribution, with correlation coefficients increasing from 0.77 to 0.81 and MAE decreasing by 18 % for ozone concentrations.

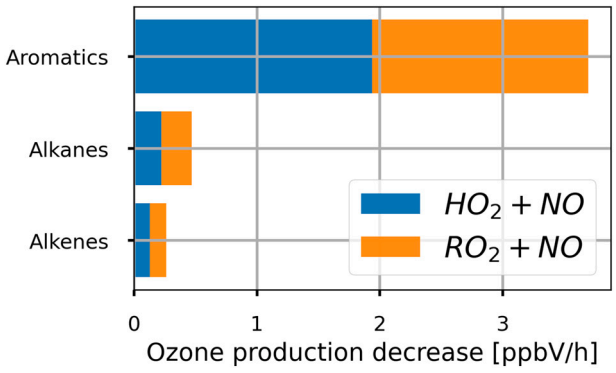

Fig. 4. Diagnostic analysis of 3D model bias impact on ozone production rates. Box model simulations constrained by 3D CTM outputs versus observations show decreased ozone production via $HO_2 + NO$ (blue) and $RO_2 + NO$ (orange) pathways. Larger decreases indicate greater model underestimation of precursor concentrations for each VOC category.

3.2. Role of aromatics in ozone production

To identify the primary drivers of ozone underestimation, we quantified individual VOC contributions to photochemical ozone production. The box model simulations using the MCM indicate reactive aromatics as the dominant contributor to ozone production at the OPECE site (Fig. S3). ARO2 (high-reactivity aromatics with OH rate constants $>1 \times 10^{-11}$ cm^3 $molecule^{-1}$ s^{-1}) accounts for 63 % of total ozone production, with ARO1 (low-reactivity aromatics with OH rate constants $<1 \times 10^{-11}$ cm^3 $molecule^{-1}$ s^{-1}) contributing an additional 10 %. Together, these aromatics represent 73 % of total ozone production. These contributions arise about equally via the $HO_2 + NO$ and $RO_2 + NO$ reaction pathways. The five most important VOCs identified by the MCM are 3-ethyltoluene (11 %), propene (10 %), 1,2,4-trimethylbenzene (7 %), o-xylene (5 %), and 4-ethyltoluene (4 %). Notably, four of these five compounds are aromatic species, underscoring their critical role in springtime ozone formation.

To evaluate the ozone underestimation by the 3-D CTM shown in Fig. 3, we compare ozone production rates from box model simulations constrained by either CTM outputs or the observations used in the base case scenario. This model evaluation indicated that the largest 3-D model bias in ozone production stems from aromatic compounds, with the model similarly underestimating ozone production rates from both $HO_2 + NO$ and $RO_2 + NO$ reaction pathways (Fig. 4). The 3-D model significantly underestimates daytime average ARO2 (−2.08 ppbV) @@@ and ARO1 (−0.69 ppbV) concentrations compared to observations (Fig. S4), which directly translates to the ozone production deficits shown in Fig. 4. We further examined the model representation of key OVOCs that contribute significantly to ozone production. As identified by Qu et al. (2021), formaldehyde, methylglyoxal, diacetyl, and glyoxal are the four most important OVOCs for ozone production in this region. Fig. S5 shows the underestimation of these critical OVOCs, primarily originating from underpredicted reactive aromatics. This connection between aromatics and OVOC underestimation provides corroborating evidence that insufficient aromatics concentrations in the model lead to reduced photochemical reactivity, thereby explaining the observed ozone underestimation.

3.3. Emission adjustments and their chemical regime impacts

We applied PMF analysis to examine the sources of reactive aromatics to improve aromatics emissions in model simulations. Fig. 5 indicates that petrochemical manufacturing (e.g., plastics) and solvent-

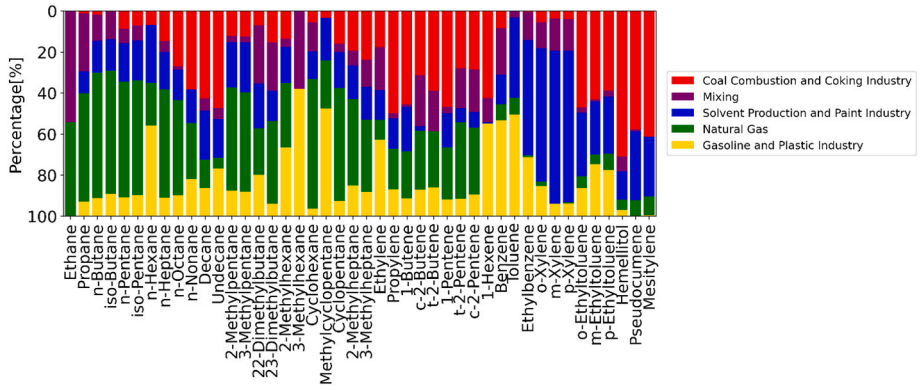

Fig. 5. Source apportionment of VOCs using PMF analysis. Stacked bar chart showing the percentage contribution of different emission sources to individual VOC species concentrations. Each bar represents 100 % of the measured concentration for a specific VOC compound, with colored segments indicating the relative contribution from coal combustion and coking industry (red), mixing processes (purple), solvent production and paint industry (green), natural gas (blue), and plastic and gasoline industry (yellow) sources.

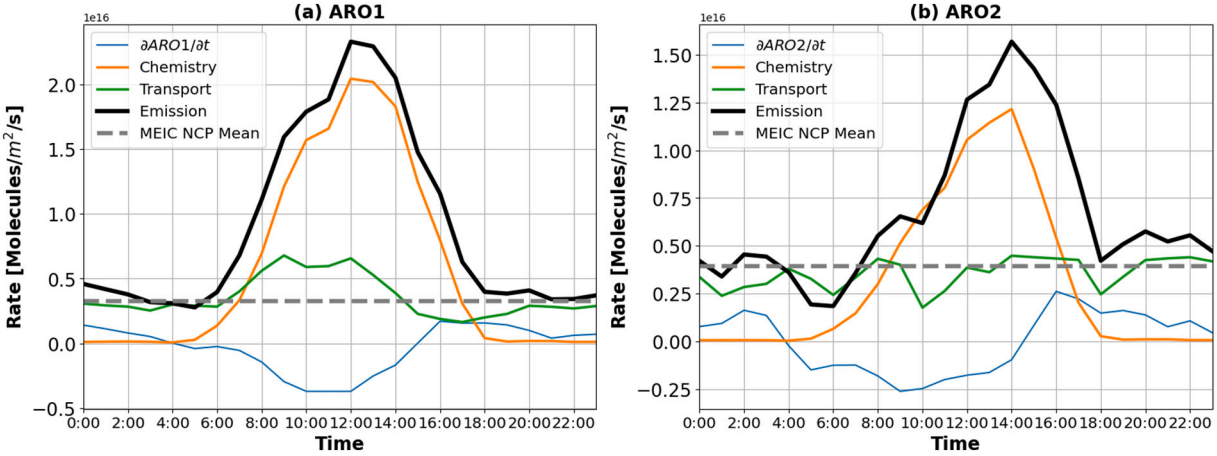

Fig. 6. Diurnal profiles of aromatics emission rates and budget terms from box model analysis of OPECE observations. The profiles for (a) ARO1 and (b) ARO2 budget components include local concentration change (light blue line), chemical loss (orange line), transport (green line), calculated emission rate (black line), and MEIC regional average emission rate (gray dashed line).

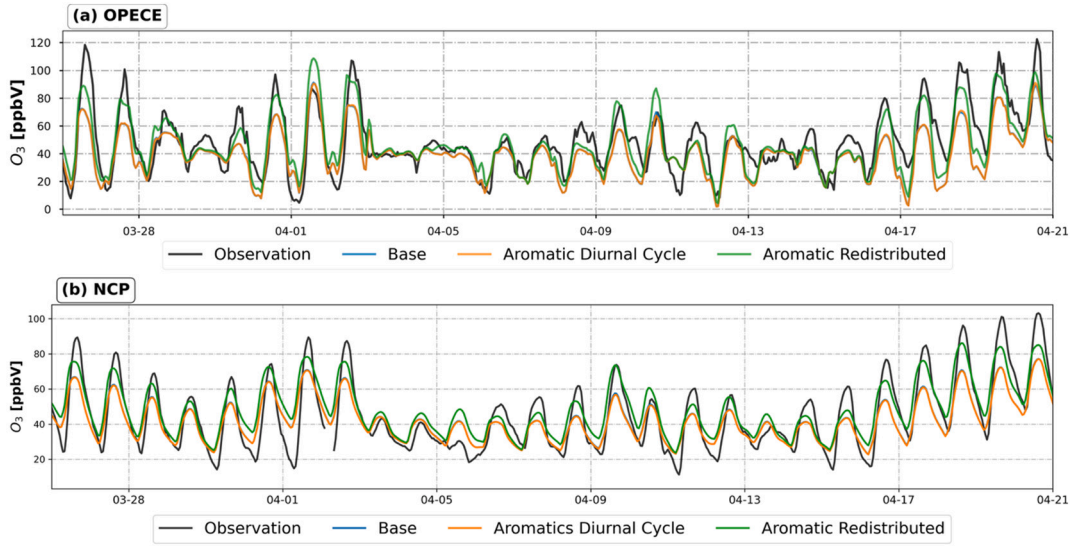

Fig. 7. Time series comparison of observed and simulated ozone concentrations showing improved model performance through observation-constrained aromatics emission modifications. (a) Time series of ozone concentrations at the OPECE site from late March to mid-April comparing site observations (black line) with model simulations using baseline emissions (blue line), observation-constrained aromatics diurnal cycles (orange line), and aromatics emission redistribution based on industrial source patterns (green line). (b) Regional mean ozone concentrations across the North China Plain showing the same simulation comparisons as panel (a).

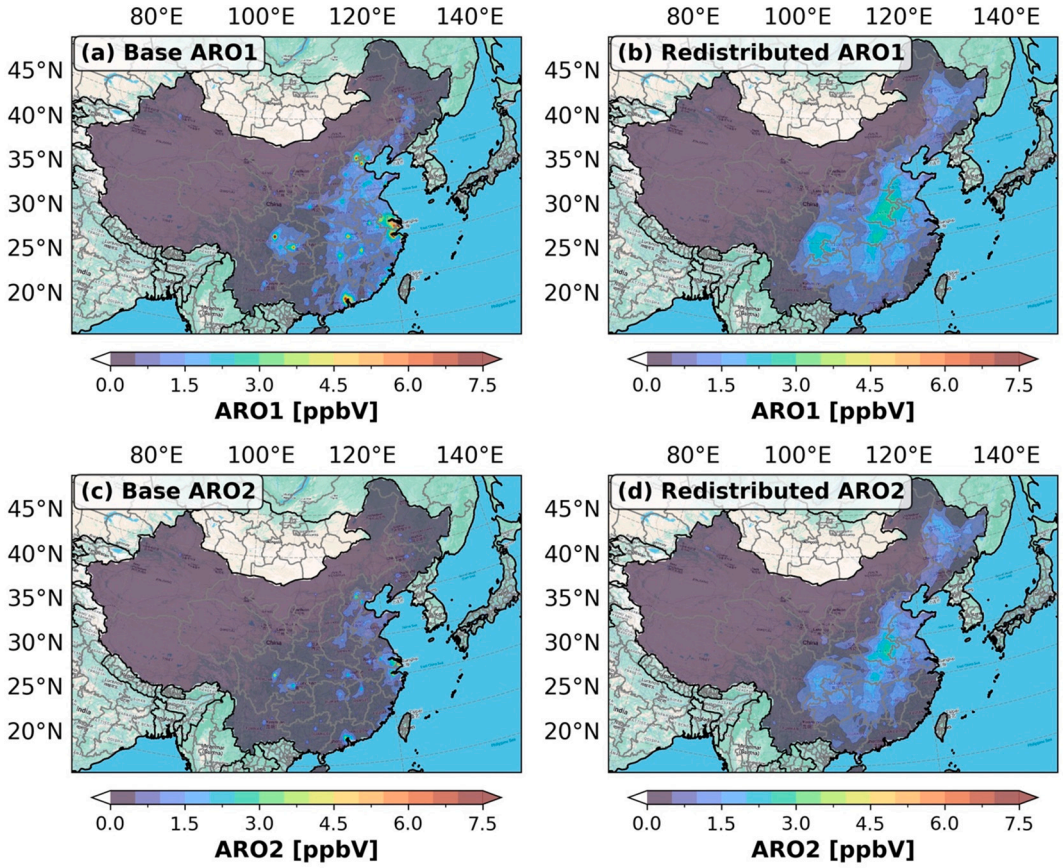

Fig. 8. Spatial distribution of reactive aromatics concentrations before and after emission redistribution across East Asia. (a) Baseline ARO1 concentrations, (b) redistributed ARO1 concentrations, (c) baseline ARO2 concentrations, and (d) redistributed ARO2 concentrations.

based industrial processes are the primary sources of ethylbenzene and xylenes, both of which are lumped into ARO2 and important ozone precursors (Fig. S3). This suggests that industrial emissions of aromatics are substantially underestimated in current inventories.

The industrial source dominated reactive aromatics emissions imply that (1) there is a diurnal cycle of aromatics emissions that are not included in the model; and (2) the spatial distributions of the aromatic emissions resemble industrial sources. We first derive the diurnal cycle of reactive aromatics emissions based on OPECE observations using Eq. (4). The resulting diurnal emission profile for each term in Eq. (4) is shown in Fig. 6. The daytime mass-balance derived emission rate is a factor of 4 higher than the nighttime rate. Implementing the observation-constrained diurnal aromatics emission profile yielded measurable improvements in ozone simulations. ARO1 and ARO2 concentrations increased by 29 % and 53 %, respectively, relative to the base case during daytime (Fig. 7).

To demonstrate that transport processes and NOx emissions are adequately represented in our simulations, we evaluated model performance for NO_2 at the OPECE site. The model shows good temporal correlation (R = 0.7) and good agreement during nighttime periods (18:00–6:00 local time), when NO_2 concentrations are controlled primarily by emissions and transport rather than photochemistry. Observed nighttime NO_2 averages 11.18 ppbV while the model simulates 10.79 ppbV, yielding only a 3.5 % mean difference. Fig. 7 provides compelling evidence that the ozone underestimation is photochemically driven rather than caused by background composition, stratosphere-troposphere exchange, or long-range transport. The baseline simulation (blue line) closely tracks observed nighttime ozone concentrations, while underestimation occurs predominantly during daytime with biases of 20–40 ppbV from midday to afternoon periods in high-ozone episodes. This diurnal pattern is diagnostic of the bias source: boundary conditions or transport would cause persistent day-night biases, while stratospheric intrusions would elevate ozone throughout the diurnal cycle. Inspection of potential vorticity (PV) in ERA5 confirms no high-PV air masses at 500 hPa when model underestimation exceeds 20 ppbV, ruling out stratospheric intrusions. The fact that nighttime ozone is well-simulated but daytime ozone is severely underestimated directly points to deficiencies in daytime photochemical production. Our box model analysis (Fig. 4) attributes this deficit to underestimated reactive aromatics, which drive ozone formation through OH-initiated oxidation during sunlit hours. Implementing observation-constrained aromatics diurnal cycles (orange line) and spatial redistribution (green line) progressively improves daytime ozone simulation while maintaining good nighttime agreement, confirming that aromatics emissions are the limiting factor.

Fig. 6 also shows that MEIC aromatics emissions for the NCP region are approximately a factor of two lower than our observation-constrained values during daytime, while nighttime emissions are comparable, implying either the MEIC aromatics emissions are too low or the spatial distributions of emissions are biased. An examination of MEIC aromatics emission distributions reveals highly concentrated distributions around urban centers. We find that the primary OVOC emissions, which are also released from solvent use and industrial sources (Mo et al., 2016; Wang et al., 2023), have much more spatially distributed emissions than aromatics in MEIC. Since the more spatially spread emissions can help correct the model underestimation at the remote OPECE site (Fig. 7, Fig. S4), we redistributed MEIC reactive aromatics emissions with the observation-constrained diurnal profiles and the spatial distribution of MEIC OVOC emissions.

Reactive aromatics are major precursors of glyoxal. Based on satellite

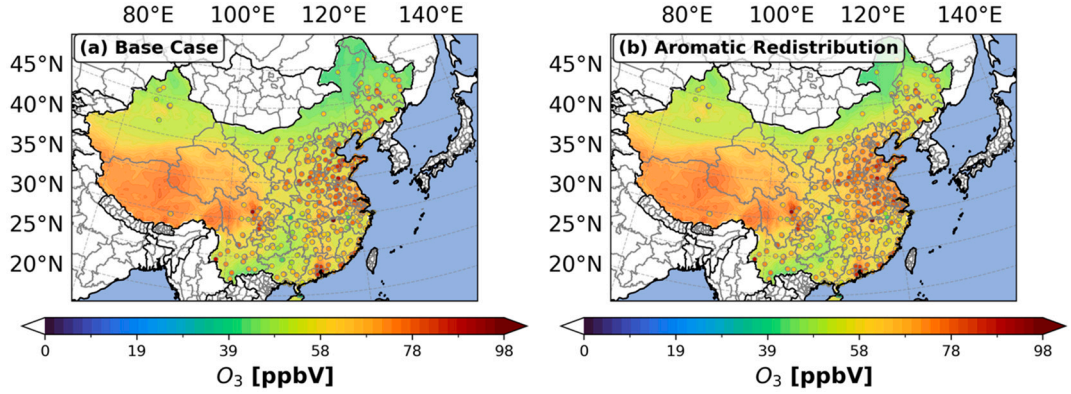

Fig. 9. Spatial distribution of ozone concentrations before and after aromatic emission redistribution across East Asia. (a) Baseline case and (b) aromatic redistribution case showing ozone mixing ratios. Filled contours represent model simulations and colored dots show CNEMC observational data.

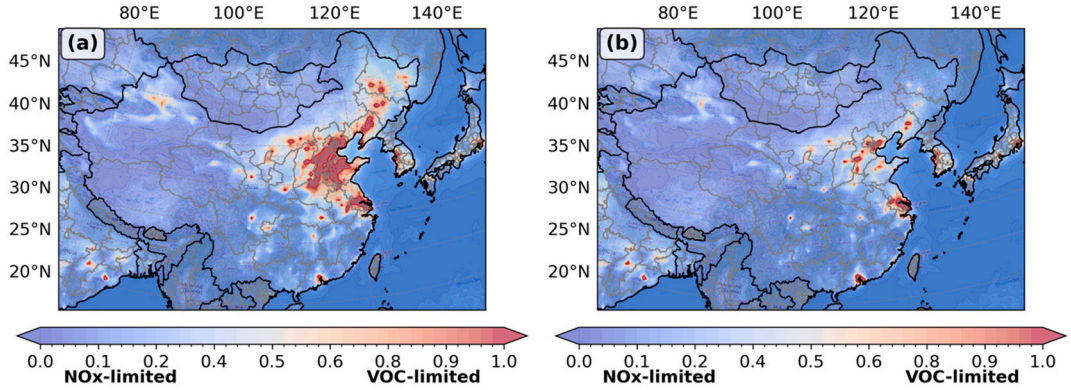

Fig. 10. Spatial distribution of photochemical regime indicator (I_{Regime}) before and after aromatics emission redistribution. The left panel shows base case I_{Regime} values with the original MEIC emissions and the right panel shows I_{Regime} values with redistributed aromatics emissions. Color scale ranges from 0.0 to 1.0, with blue colors indicating NOx-limited conditions and red colors indicating VOC-limited conditions for ozone formation.

observations of glyoxal (Lerot et al., 2021; Liu et al., 2012a; Zhang et al., 2017), Lerot et al. (2021) reported high glyoxal columns over the NCP region in spring. The MEIC emission redistributions led to relatively low reactive aromatic concentrations over the NCP region (Fig. S4) and consequently low glyoxal columns in the region (Fig. S6). The redistributed emissions significantly increased both reactive aromatics and glyoxal columns in this region, achieving better agreement with satellite-observed spatial patterns and providing an independent validation of our emission adjustments.

The spatiotemporal redistributions of aromatics emissions improved model performance substantially. ARO1 daytime concentrations increased by 43 % from the base case, while ARO2 concentrations increased five-fold at the OPECE site, improving the model simulation of reactive aromatics (Fig. S4). The much larger increase in ARO2 than ARO1 is due to much more urban-centric emissions of the former in the MEIC inventories. Fig. 8 shows that simulated high ARO1 and ARO2

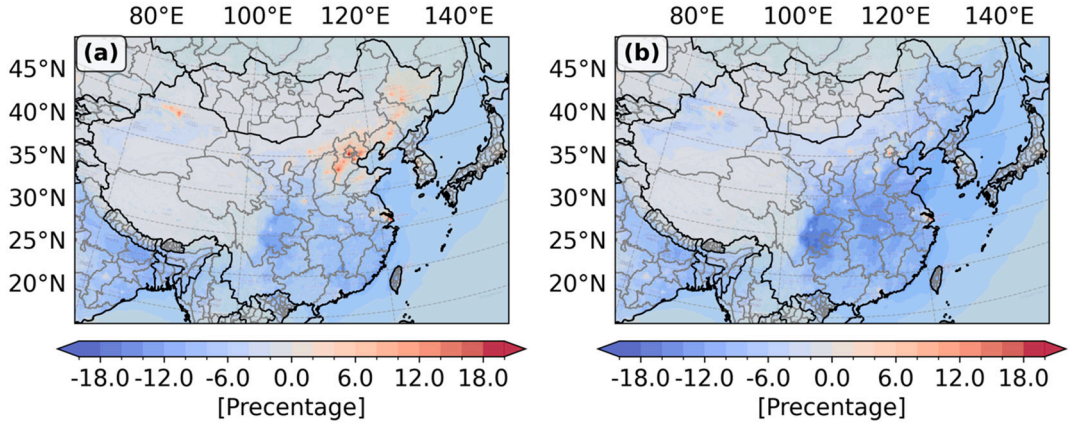

Fig. 11. Ozone changes due to 50 % reduction of NO_x emissions: (a) base case with the MEIC emissions and (b) with redistributed aromatics emissions. Color scale ranges from −18 % to +18 %, with blue colors indicating negative ozone response (NO_x-limited regime) and red colors indicating positive ozone response (VOC-limited regime) to NO_x emission reductions.

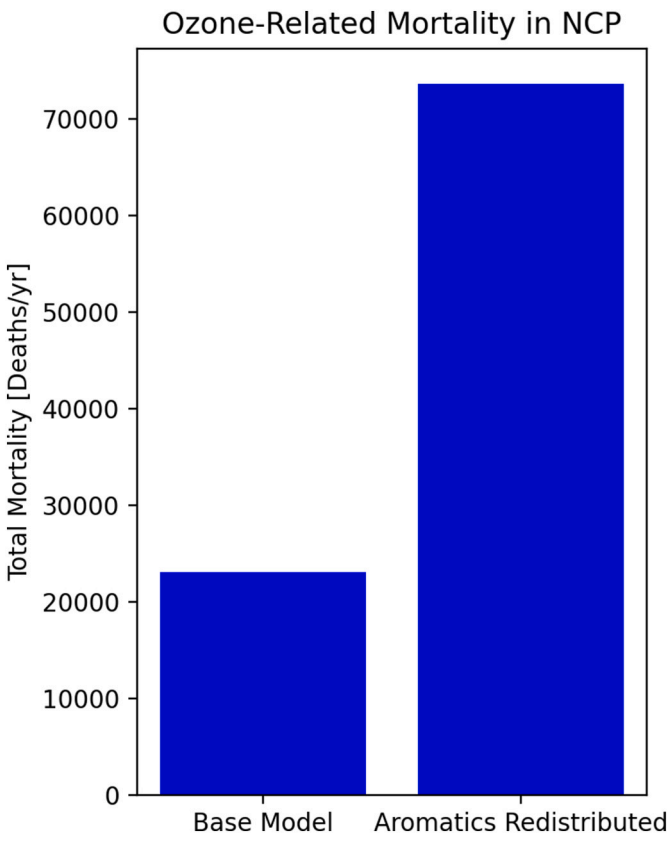

Fig. 12. Annual ozone-related premature mortality estimates in the NCP region for base emission inventory versus aromatics-redistributed scenarios. The aromatics-redistributed scenario incorporates observation-constrained aromatics emissions to account for previously underestimated aromatics contributions to ozone formation.

concentrations are concentrated around urban regions using the MEIC emissions. After emission redistributions, ARO1 and ARO2 are both much more dispersed over eastern China. Since Fig. S4 still shows some underestimations of ARO1 and ARO2 at the OPECE site, increasing aromatics emissions in urban areas will further improve model simulation results. We limited the scope of this work to regional emission patterns of aromatics emissions since we do not have concurrent aromatics measurements in urban regions. Further improvements in aromatics emissions will require more observation constraints.

These adjustments also resulted in significant improvements in ozone simulation. Fig. 2 shows that the redistributed emissions enable the model to better capture the observed high ozone concentrations at the OPECE site. The improvement is equally significant for improving the ozone simulation over the NCP region (Fig. 9). The mean absolute error (MAE) decreased from 31 ppb to 13 ppb at the OPECE site and from 14.5 ppb to 8.3 ppb for the NCP region (Fig. S7).

The redistribution of reactive aromatics emissions has significant ramifications for effective ozone control since it fundamentally alters the photochemical regime across the NCP region. We use I_{Regime} (Eq. (2)) to diagnose the chemical regime. Prior to the redistribution of aromatics emissions, the NCP region was predominantly in the VOC-limited regime (Fig. 10). Under this regime, a 50 % reduction of NO_x emissions leads to increasing ozone over the NCP region (Fig. 11). Following the redistributions of aromatics emissions, most of the NCP region is in a transition zone towards NO_x-limited regime except several urban centers (Fig. 10). A 50 % reduction of NOx emissions leads to decreasing ozone over the NCP region except a few urban areas (Fig. 11). This characterization aligns with previous studies of summer chemical regimes in the NCP region (Li et al., 2021c; Qiao et al., 2024; Zhu et al., 2023). This shift to a transitional regime has critical implications for ozone control strategies in the NCP region. In the transitional regime, ozone formation is sensitive to both NOx and VOC concentrations, meaning that reductions in either precursor type can effectively reduce ozone without the adverse effects seen in purely VOC-limited conditions (e.g., Liu et al., 2012b). Unlike the VOC-limited regime where NOx reductions can paradoxically increase ozone due to reduced ozone titration, the transitional regime allows beneficial responses to NOx controls while maintaining responsiveness to VOC reductions. This finding suggests that coordinated reductions of both NOx and VOCs represent the most effective approach for ozone control across most of the NCP region.

To evaluate the public health implications of redistributed aromatics emissions, we calculated secondary ozone-related premature mortality attributable to aromatics-induced ozone formation. Following established methodologies (Achebak et al., 2024; Bell et al., 2006; Li et al., 2023; Lin et al., 2018), we estimated premature mortality for both base case and aromatics-redistributed scenarios. It is important to note that we focus specifically on the secondary health impacts through ozone formation pathways, as aromatics are important ozone precursors that contribute to O_3 production through photochemical reactions. The aromatics-redistributed scenario, constrained by observations, reveals the previously underestimated contribution of aromatics to secondary ozone formation and its associated health burden. The spatial distribution of secondary premature mortality reveals that the secondary effects of aromatics emission redistributions increase ozone-related premature mortality over the NCP region (Fig. S8). The regional total increases by a factor of 2–3, corresponding to approximately 50,000 additional deaths annually in the NCP region (Fig. 12). These findings highlight the substantial secondary health impacts of aromatics emissions and underscore the potential health benefits of targeting aromatics emission controls to reduce both primary and secondary air pollution impacts.

4. Conclusions

This study demonstrates that reactive aromatic compounds are the dominant driver of elevated springtime ozone concentrations across the North China Plain (NCP), which substantially exceeded levels observed in polluted regions of California. While capturing the observed ozone level over the U.S., the model fails to simulate the observed high ozone concentrations over eastern China. Using observations from the remote coastal OPECE site, we find that reactive aromatics account for 73 % of photochemical ozone production. 3-D model simulations using the MEIC emission inventories underestimate ozone concentrations by 5 % to 22 % at the OPECE site and the broad NCP region. Budget analysis of the VOC measurements at the OPECE site indicates a large diurnal variation in reactive aromatics emissions with daytime emissions a factor of three higher than at night. Furthermore, modeling analysis reveals that MEIC reactive aromatics emissions have concentrated distributions around urban centers. Both OPECE aromatics measurements and satellite observations of glyoxal indicate broad regional emission distributions. The current inventory likely underestimates or misallocates reactive aromatics emissions from plastic manufacturing and solvent-based industries. The spatiotemporal redistributions of reactive aromatics emissions greatly improved the simulations of reactive aromatics and ozone concentrations at the OPECE site and the ozone distribution over the NCP region, significantly reduced the model's ozone low biases in the spring.

The redistribution of reactive aromatics emissions has significant ramifications for effective ozone control. With the MEIC emissions, most of the NCP region is in the VOC-limited regime. Reducing NO_x emissions tends to increase ozone concentrations. However, after the spatiotemporal redistribution of reactive aromatics emissions, much of the NCP region shifted into a transition zone towards the NO_x-limited regime except a few urban areas. Reducing NO_x emissions decreased NCP regional ozone concentrations, indicating that effective ozone control strategies must target both precursor types rather than focusing

exclusively on VOC reductions. The emission redistribution also has important public health implications. With the same emission total but different distribution, aromatics-induced ozone formation causes an additional 50,000 premature deaths annually over the NCP region. These findings underscore the urgent need for improving the characterization and control of reactive aromatics emissions in rapidly developing regions, where the spatial expansion of industrial activities beyond traditional urban centers poses increasing challenges for air quality management and public health protection. Future research incorporating facility-level emission data and expanded measurement networks across urban-industrial gradients will further refine emission redistribution methodologies and improve understanding of spatial emission variability within rapidly industrializing regions.

CRediT authorship contribution statement

Fanghe Zhao: Writing – review & editing, Writing – original draft, Visualization, Validation, Software, Methodology, Formal analysis, Data curation, Conceptualization. **Yuhang Wang:** Writing – review & editing, Supervision, Project administration, Funding acquisition, Conceptualization. **Lewis Gregory Huey:** Supervision, Project administration, Funding acquisition. **Shengjun Xi:** Writing – review & editing. **Young Ro Lee:** Writing – review & editing, Resources, Investigation, Formal analysis, Data curation. **Wei Song:** Resources, Investigation, Data curation. **Xinming Wang:** Resources, Investigation, Data curation. **Jianhui Tang:** Resources, Investigation, Data curation. **Kezhen Chong:** Formal analysis. **Hang Qu:** Formal analysis.

Declaration of competing interest

The authors declare that they have no known competing financial interests or personal relationships that could have appeared to influence the work reported in this paper.

Acknowledgments

This work was supported in part by the National Science Foundation Atmospheric Chemistry Program under Grant No. 1743401. This research was supported in part through research cyberinfrastructure resources and services provided by the Partnership for an Advanced Computing Environment (PACE) at the Georgia Institute of Technology, Atlanta, Georgia, USA. The authors thank the science team for the OPECE 2018 campaign.

Appendix A. Supplementary data

Supplementary data to this article can be found online at https://doi.org/10.1016/j.scitotenv.2025.180909.

Data availability

Data will be made available on request.

References

Achebak, H., Garatachea, R., Pay, M.T., Jorba, O., Guevara, M., Pérez García-Pando, C., Ballester, J., 2024. Geographic sources of ozone air pollution and mortality burden in Europe. Nat. Med. 30 (6), 1732–1738. https://doi.org/10.1038/s41591-024-02976-x.

Bell, M.L., Peng, R.D., Dominici, F., 2006. The exposure-response curve for ozone and risk of mortality and the adequacy of current ozone regulations. Environ. Health Perspect. 114 (4), 532–536. https://doi.org/10.1289/ehp.8816.

Brown, S.G., Eberly, S., Paatero, P., Norris, G.A., 2015. Methods for estimating uncertainty in PMF solutions: examples with ambient air and water quality data and guidance on reporting PMF results. Sci. Total Environ. 518–519, 626–635. https://doi.org/10.1016/j.scitotenv.2015.01.022.

Cai, C., Geng, F., Tie, X., Yu, Q., An, J., 2010. Characteristics and source apportionment of VOCs measured in Shanghai, China. Atmos. Environ. 44 (38), 5005–5014. https://doi.org/10.1016/j.atmosenv.2010.07.059.

Carter, W.P.L., 2010. Development of the SAPRC-07 chemical mechanism. Atmos. Environ. 44 (40), 5324–5335. https://doi.org/10.1016/j.atmosenv.2010.01.026.

Cheng, J., Tong, D., Zhang, Q., Liu, Y., Lei, Y., Yan, G., Yan, L., Yu, S., Cui, R.Y., Clarke, L., Geng, G., Zheng, B., Zhang, X., Davis, S.J., He, K., 2021. Pathways of China's $PM_{2.5}$ air quality 2015–2060 in the context of carbon neutrality. Natl. Sci. Rev. 8 (12), nwab078. https://doi.org/10.1093/nsr/nwab078.

Cheng, J., Tong, D., Liu, Y., Geng, G., Davis, S.J., He, K., Zhang, Q., 2023. A synergistic approach to air pollution control and carbon neutrality in China can avoid millions of premature deaths annually by 2060. One Earth 6 (8), 978–989. https://doi.org/10.1016/j.oneear.2023.07.007.

China National Environmental Monitoring Center Network, 2018. http://www.cnemc.cn/.

Choi, Y., Wang, Y., Zeng, T., Cunnold, D., Yang, E.-S., Martin, R., Chance, K., Thouret, V., Edgerton, E., 2008. Springtime transitions of NO_2, CO, and O_3 over North America: model evaluation and analysis. J. Geophys. Res. Atmos. 113 (D20). https://doi.org/10.1029/2007JD009632.

Chong, K., Wang, Y., Liu, C., Gao, Y., Boersma, K.F., Tang, J., Wang, X., 2024a. Remote sensing measurements at a rural site in China: implications for satellite NO_2 and HCHO measurement uncertainty and emissions from fires. J. Geophys. Res. Atmos. 129 (2), e2023JD039310. https://doi.org/10.1029/2023JD039310.

Chong, K., Wang, Y., Zheng, M., Qu, H., Zhang, R., Lee, Y.R., Ji, Y., Huey, L.G., Fang, H., Song, W., Fang, Z., Liu, C., Gao, Y., Tang, J., Wang, X., 2024b. Observation-based diagnostics of reactive nitrogen recycling through HONO heterogenous production: divergent implications for ozone production and emission control. Environ. Sci. Technol. 58 (26), 11554–11567. https://doi.org/10.1021/acs.est.3c07967.

Cohen, A.J., Brauer, M., Burnett, R., Anderson, H.R., Frostad, J., Estep, K., Balakrishnan, K., Brunekreef, B., Dandona, L., Dandona, R., Feigin, V., Freedman, G., Hubbell, B., Jobling, A., Kan, H., Knibbs, L., Liu, Y., Martin, R., Morawska, L., Forouzanfar, M.H., 2017. Estimates and 25-year trends of the global burden of disease attributable to ambient air pollution: an analysis of data from the Global Burden of Diseases Study 2015. Lancet 389 (10082), 1907–1918. https://doi.org/10.1016/S0140-6736(17)30505-6.

Demetillo, M.A.G., Anderson, J.F., Geddes, J.A., Yang, X., Najacht, E.Y., Herrera, S.A., Kabasares, K.M., Kotsakis, A.E., Lerdau, M.T., Pusede, S.E., 2019. Observing severe drought influences on ozone air pollution in California. Environ. Sci. Technol. 53 (9), 4695–4706. https://doi.org/10.1021/acs.est.8b04852.

Fu, Y., Liao, H., Yang, Y., 2019. Interannual and decadal changes in tropospheric ozone in China and the associated chemistry-climate interactions: a review. Adv. Atmos. Sci. 36 (9), 975–993. https://doi.org/10.1007/s00376-019-8216-9.

Guenther, A.B., Jiang, X., Heald, C.L., Sakulyanontvittaya, T., Duhl, T., Emmons, L.K., Wang, X., 2012. The Model of Emissions of Gases and Aerosols from Nature version 2.1 (MEGAN2.1): an extended and updated framework for modeling biogenic emissions. Geosci. Model Dev. 5 (6), 1471–1492. https://doi.org/10.5194/gmd-5-1471-2012.

Hao, S., Du, Q., Wei, X., Yan, H., Zhang, M., Sun, Y., Liu, S., Fan, L., Zhang, G., 2024. Composition and reactivity of volatile organic compounds and the implications for ozone formation in the North China Plain. Atmosphere 15 (2), 213 https://www.mdpi.com/2073-4433/15/2/213.

Hersbach, H., Bell, B., Berrisford, P., Hirahara, S., Horányi, A., Muñoz-Sabater, J., Nicolas, J., Peubey, C., Radu, R., Schepers, D., Simmons, A., Soci, C., Abdalla, S., Abellan, X., Balsamo, G., Bechtold, P., Biavati, G., Bidlot, J., Bonavita, M., Thépaut, J.-N., 2020. The ERA5 global reanalysis. Q. J. R. Meteorol. Soc. 146 (730), 1999–2049. https://doi.org/10.1002/qj.3803.

Huang, M., Bowman, K.W., Carmichael, G.R., Bradley Pierce, R., Worden, H.M., Luo, M., Cooper, O.R., Pollack, I.B., Ryerson, T.B., Brown, S.S., 2013. Impact of Southern California anthropogenic emissions on ozone pollution in the mountain states: model analysis and observational evidence from space. J. Geophys. Res. Atmos. 118 (22), 12,784–12,803. https://doi.org/10.1002/2013JD020205.

Inness, A., Ades, M., Agustí-Panareda, A., Barré, J., Benedictow, A., Blechschmidt, A.M., Dominguez, J.J., Engelen, R., Eskes, H., Flemming, J., Huijnen, V., Jones, L., Kipling, Z., Massart, S., Parrington, M., Peuch, V.H., Razinger, M., Remy, S., Schulz, M., Suttie, M., 2019. The CAMS reanalysis of atmospheric composition. Atmos. Chem. Phys. 19 (6), 3515–3556. https://doi.org/10.5194/acp-19-3515-2019.

Jenkin, M.E., Saunders, S.M., Wagner, V., Pilling, M.J., 2003. Protocol for the development of the Master Chemical Mechanism, MCM v3 (Part B): tropospheric degradation of aromatic volatile organic compounds. Atmos. Chem. Phys. 3 (1), 181–193. https://doi.org/10.5194/acp-3-181-2003.

Jenkin, M.E., Young, J.C., Rickard, A.R., 2015. The MCM v3.3.1 degradation scheme for isoprene. Atmos. Chem. Phys. 15 (20), 11433–11459. https://doi.org/10.5194/acp-15-11433-2015.

Jin, L., Tonse, S., Cohan, D.S., Mao, X., Harley, R.A., Brown, N.J., 2008. Sensitivity analysis of ozone formation and transport for a Central California air pollution episode. Environ. Sci. Technol. 42 (10), 3683–3689. https://doi.org/10.1021/es072069d.

Kleinman, L.I., 2005. The dependence of tropospheric ozone production rate on ozone precursors. Atmos. Environ. 39 (3), 575–586. https://doi.org/10.1016/j.atmosenv.2004.08.047.

Kong, L., Tang, X., Zhu, J., Wang, Z., Li, J., Wu, H., Wu, Q., Chen, H., Zhu, L., Wang, W., Liu, B., Wang, Q., Chen, D., Pan, Y., Song, T., Li, F., Zheng, H., Jia, G., Lu, M., Carmichael, G.R., 2021. A 6-year-long (2013–2018) high-resolution air quality reanalysis dataset in China based on the assimilation of surface observations from CNEMC. Earth Syst. Sci. Data 13 (2), 529–570. https://doi.org/10.5194/essd-13-529-2021.

Lee, Y., Huey, L.G., Wang, Y., Qu, H., Zhang, R., Ji, Y., Tanner, D., Wang, X., Tang, J., Song, W., 2021. Photochemistry of volatile organic compounds in the Yellow River

Delta, China: formation of O_3 and peroxyacyl nitrates. J. Geophys. Res. Atmos. 126 (23), e2021JD035296.
Lerot, C., Hendrick, F., Van Roozendael, M., Alvarado, L.M.A., Richter, A., De Smedt, I., Theys, N., Vlietinck, J., Yu, H., Van Gent, J., Stavrakou, T., Müller, J.F., Valks, P., Loyola, D., Irie, H., Kumar, V., Wagner, T., Schreier, S.F., Sinha, V., Retscher, C., 2021. Glyoxal tropospheric column retrievals from TROPOMI — multi-satellite intercomparison and ground-based validation. Atmos. Meas. Tech. 14 (12), 7775–7807. https://doi.org/10.5194/amt-14-7775-2021.
Li, J., Zhang, M., Wu, F., Sun, Y., Tang, G., 2017. Assessment of the impacts of aromatic VOC emissions and yields of SOA on SOA concentrations with the air quality model RAMS-CMAQ. Atmos. Environ. 158, 105–115. https://doi.org/10.1016/j.atmosenv.2017.03.035.
Li, J., Wang, Y., Qu, H., 2019. Dependence of summertime surface ozone on NO and VOC emissions over the United States: peak time and value. Geophys. Res. Lett. 46 (6), 3540–3550. https://doi.org/10.1029/2018GL081823.
Li, J., Wang, Y., Zhang, R., Smeltzer, C., Weinheimer, A., Herman, J., Boersma, K.F., Celarier, E.A., Long, R.W., Szykman, J.J., Delgado, R., Thompson, A.M., Knepp, T.N., Lamsal, L.N., Janz, S.J., Kowalewski, M.G., Liu, X., Nowlan, C.R., 2021b. Comprehensive evaluations of diurnal NO_2 measurements during DISCOVER-AQ 2011: effects of resolution-dependent representation of NOx emissions. Atmos. Chem. Phys. 21 (14), 11133–11160. https://doi.org/10.5194/acp-21-11133-2021.
Li, K., Jacob, D.J., Shen, L., Lu, X., De Smedt, I., Liao, H., 2020a. Increases in surface ozone pollution in China from 2013 to 2019: anthropogenic and meteorological influences. Atmos. Chem. Phys. 20 (19), 11423–11433. https://doi.org/10.5194/acp-20-11423-2020.
Li, K., Jacob, D.J., Liao, H., Qiu, Y., Shen, L., Zhai, S., Bates, K.H., Sulprizio, M.P., Song, S., Lu, X., Zhang, Q., Zheng, B., Zhang, Y., Zhang, J., Lee, H.C., Kuk, S.K., 2021a. Ozone pollution in the North China plain spreading into the late-winter haze season. Proc. Natl. Acad. Sci. 118 (10), e2015797118. https://doi.org/10.1073/pnas.2015797118.
Li, Q., Su, G., Li, C., Liu, P., Zhao, X., Zhang, C., Sun, X., Mu, Y., Wu, M., Wang, Q., Sun, B., 2020b. An investigation into the role of VOCs in SOA and ozone production in Beijing, China. Sci. Total Environ. 720, 137536. https://doi.org/10.1016/j.scitotenv.2020.137536.
Li, R., Xu, M., Li, M., Chen, Z., Zhao, N., Gao, B., Yao, Q., 2021c. Identifying the spatiotemporal variations in ozone formation regimes across China from 2005 to 2019 based on polynomial simulation and causality analysis. Atmos. Chem. Phys. 21 (20), 15631–15646. https://doi.org/10.5194/acp-21-15631-2021.
Li, Y., Lau, A.K.H., Fung, J.C.H., Zheng, J., Liu, S., 2013. Importance of NOx control for peak ozone reduction in the Pearl River Delta region. J. Geophys. Res. Atmos. 118 (16), 9428–9443. https://doi.org/10.1002/jgrd.50659.
Li, Y., Ma, L., Ni, M., Bai, Y., Li, C., 2023. Drivers of ozone-related premature mortality in China: implications for historical and future scenarios. J. Environ. Manag. 345, 118663. https://doi.org/10.1016/j.jenvman.2023.118663.
Liaskoni, M., Huszár, P., Bartík, L., Prieto Perez, A.P., Karlický, J., Šindelářová, K., 2024. The long-term impact of biogenic volatile organic compound emissions on urban ozone patterns over central Europe: contributions from urban and rural vegetation. Atmos. Chem. Phys. 24 (23), 13541–13569. https://doi.org/10.5194/acp-24-13541-2024.
Lin, Y., Jiang, F., Zhao, J., Zhu, G., He, X., Ma, X., Li, S., Sabel, C.E., Wang, H., 2018. Impacts of O_3 on premature mortality and crop yield loss across China. Atmos. Environ. 194, 41–47. https://doi.org/10.1016/j.atmosenv.2018.09.024.
Liu, H., Liu, S., Xue, B., Lv, Z., Meng, Z., Yang, X., Xue, T., Yu, Q., He, K., 2018. Ground-level ozone pollution and its health impacts in China. Atmos. Environ. 173, 223–230. https://doi.org/10.1016/j.atmosenv.2017.11.014.
Liu, Z., Wang, Y., Gu, D., Zhao, C., Huey, L.G., Stickel, R., Liao, J., Shao, M., Zhu, T., Zeng, L., Amoroso, A., Costabile, F., Chang, C.C., Liu, S.C., 2012a. Summertime photochemistry during CAREBeijing-2007: ROx budgets and O_3 formation. Atmos. Chem. Phys. 12 (16), 7737–7752. https://doi.org/10.5194/acp-12-7737-2012.
Liu, Z., Wang, Y., Vrekoussis, M., Richter, A., Wittrock, F., Burrows, J.P., Shao, M., Chang, C.-C., Liu, S.-C., Wang, H., Chen, C., 2012b. Exploring the missing source of glyoxal (CHOCHO) over China. Geophys. Res. Lett. 39 (10). https://doi.org/10.1029/2012GL051645.
Lu, X., Hong, J., Zhang, L., Cooper, O.R., Schultz, M.G., Xu, X., Wang, T., Gao, M., Zhao, Y., Zhang, Y., 2018. Severe surface ozone pollution in China: a global perspective. Environ. Sci. Technol. Lett. 5 (8), 487–494. https://doi.org/10.1021/acs.estlett.8b00366.
Lyu, X., Wang, N., Guo, H., Xue, L., Jiang, F., Zeren, Y., Cheng, H., Cai, Z., Han, L., Zhou, Y., 2019. Causes of a continuous summertime O_3 pollution event in Jinan, a central city in the North China Plain. Atmos. Chem. Phys. 19 (5), 3025–3042. https://doi.org/10.5194/acp-19-3025-2019.
Mazzuca, G.M., Ren, X., Loughner, C.P., Estes, M., Crawford, J.H., Pickering, K.E., Weinheimer, A.J., Dickerson, R.R., 2016. Ozone production and its sensitivity to NO_x and VOCs: results from the DISCOVER-AQ field experiment, Houston 2013. Atmos. Chem. Phys. 16 (22), 14463–14474. https://doi.org/10.5194/acp-16-14463-2016.
Mo, Z., Shao, M., Lu, S., 2016. Compilation of a source profile database for hydrocarbon and OVOC emissions in China. Atmos. Environ. 143, 209–217. https://doi.org/10.1016/j.atmosenv.2016.08.025.
Ni, R., Lin, J., Yan, Y., Lin, W., 2018. Foreign and domestic contributions to springtime ozone over China. Atmos. Chem. Phys. 18 (15), 11447–11469. https://doi.org/10.5194/acp-18-11447-2018.
Oliveira, K., Guevara, M., Jorba, O., Petetin, H., Bowdalo, D., Tena, C., Montané Pinto, G., López, F., Pérez García-Pando, C., 2024. On the uncertainty of anthropogenic aromatic volatile organic compound emissions: model evaluation and sensitivity analysis. Atmos. Chem. Phys. 24 (12), 7137–7177. https://doi.org/10.5194/acp-24-7137-2024.
Punger, E.M., West, J.J., 2013. The effect of grid resolution on estimates of the burden of ozone and fine particulate matter on premature mortality in the United States. Air Qual. Atmos. Health 6 (3). https://doi.org/10.1007/s11869-013-0197-8.
Qiao, W., Li, K., Yang, Z., Chen, L., Liao, H., 2024. Implications of the extremely hot summer of 2022 on urban ozone control in China. Atmos. Ocean. Sci. Lett. 17 (6), 100470. https://doi.org/10.1016/j.aosl.2024.100470.
Qu, H., Wang, Y., Zhang, R., Li, J., 2020. Extending ozone-precursor relationships in China from peak concentration to peak time. J. Geophys. Res. Atmos. 125 (22), e2020JD033670. https://doi.org/10.1029/2020JD033670.
Qu, H., Wang, Y., Zhang, R., Liu, X., Huey, L.G., Sjostedt, S., Zeng, L., Lu, K., Wu, Y., Shao, M., Hu, M., Tan, Z., Fuchs, H., Broch, S., Wahner, A., Zhu, T., Zhang, Y., 2021. Chemical production of oxygenated volatile organic compounds strongly enhances boundary-layer oxidation chemistry and ozone production. Environ. Sci. Technol. 55 (20), 13718–13727. https://doi.org/10.1021/acs.est.1c04489.
Seinfeld, J.H., Pandis, S.N., 2016. Atmospheric Chemistry and Physics: From Air Pollution to Climate Change, Third ed. John Wiley & Sons, Inc.
Tanaka, S., 2015. Environmental regulations on air pollution in China and their impact on infant mortality. J. Health Econ. 42, 90–103. https://doi.org/10.1016/j.jhealeco.2015.02.004.
Tong, D., Cheng, J., Liu, Y., Yu, S., Yan, L., Hong, C., Qin, Y., Zhao, H., Zheng, Y., Geng, G., Li, M., Liu, F., Zhang, Y., Zheng, B., Clarke, L., Zhang, Q., 2020. Dynamic projection of anthropogenic emissions in China: methodology and 2015–2050 emission pathways under a range of socio-economic, climate policy, and pollution control scenarios. Atmos. Chem. Phys. 20 (9), 5729–5757. https://doi.org/10.5194/acp-20-5729-2020.
Wang, H., Yan, R., Xu, T., Wang, Y., Wang, Q., Zhang, T., An, J., Huang, C., Gao, Y., Gao, Y., Li, X., Yu, C., Jing, S., Qiao, L., Lou, S., Tao, S., Li, Y., 2020. Observation constrained aromatic emissions in Shanghai, China. J. Geophys. Res. Atmos. 125 (6), e2019JD031815. https://doi.org/10.1029/2019JD031815.
Wang, S., Zhang, J., Zhang, Y., Wang, L., Sun, Z., Wang, H., 2023. Review on source profiles of volatile organic compounds (VOCs) in typical industries in China. Atmosphere 14 (5), 878 https://www.mdpi.com/2073-4433/14/5/878.
Wang, X., Zhao, W., Zhang, T., Qiu, Y., Ma, P., Li, L., Wang, L., Wang, M., Zheng, D., Zhao, W., 2022. Analysis of the characteristics of ozone pollution in the North China Plain from 2016 to 2020. Atmosphere 13 (5), 715 https://www.mdpi.com/2073-4433/13/5/715.
Wang, Y., Ridley, B., Fried, A., Cantrell, C., Davis, D., Chen, G., Snow, J., Heikes, B., Talbot, R., Dibb, J., Flocke, F., Weinheimer, A., Blake, N., Blake, D., Shetter, R., Lefer, B., Atlas, E., Coffey, M., Walega, J., Wert, B., 2003. Springtime photochemistry at northern mid and high latitudes. J. Geophys. Res. Atmos. 108 (D4). https://doi.org/10.1029/2002JD002227.
Wu, R., Xie, S., 2017. Spatial distribution of ozone formation in China derived from emissions of speciated volatile organic compounds. Environ. Sci. Technol. 51 (5), 2574–2583. https://doi.org/10.1021/acs.est.6b03634.
Xue, L.K., Wang, T., Gao, J., Ding, A.J., Zhou, X.H., Blake, D.R., Wang, X.F., Saunders, S. M., Fan, S.J., Zuo, H.C., Zhang, Q.Z., Wang, W.X., 2014. Ground-level ozone in four Chinese cities: precursors, regional transport and heterogeneous processes. Atmos. Chem. Phys. 14 (23), 13175–13188. https://doi.org/10.5194/acp-14-13175-2014.
Yan, Q., Wang, Y., Cheng, Y., Li, J., 2021. Summertime clean-background ozone concentrations derived from ozone precursor relationships are lower than previous estimates in the southeast United States. Environ. Sci. Technol. 55 (19), 12852–12861. https://doi.org/10.1021/acs.est.1c03035.
Yan, Y., Cabrera-Perez, D., Lin, J., Pozzer, A., Hu, L., Millet, D.B., Porter, W.C., Lelieveld, J., 2019. Global tropospheric effects of aromatic chemistry with the SAPRC-11 mechanism implemented in GEOS-Chem version 9-02. Geosci. Model Dev. 12 (1), 111–130. https://doi.org/10.5194/gmd-12-111-2019.
Yang, Y., Wang, Y., Huang, W., Yao, D., Zhao, S., Wang, Y., Ji, D., Zhang, R., Wang, Y., 2021. Parameterized atmospheric oxidation capacity and speciated OH reactivity over a suburban site in the North China Plain: a comparative study between summer and winter. Sci. Total Environ. 773, 145264. https://doi.org/10.1016/j.scitotenv.2021.145264.
Yue, X., Unger, N., 2014. Ozone vegetation damage effects on gross primary productivity in the United States. Atmos. Chem. Phys. 14 (17), 9137–9153. https://doi.org/10.5194/acp-14-9137-2014.
Zhang, J., Wei, Y., Fang, Z., 2019. Ozone pollution: a major health hazard worldwide [review]. Front. Immunol. 10, 2019. https://doi.org/10.3389/fimmu.2019.02518.
Zhang, K., Li, L., Huang, L., Wang, Y., Huo, J., Duan, Y., Wang, Y., Fu, Q., 2020. The impact of volatile organic compounds on ozone formation in the suburban area of Shanghai. Atmos. Environ. 232, 117511. https://doi.org/10.1016/j.atmosenv.2020.117511.
Zhang, R., Wang, Y., He, Q., Chen, L., Zhang, Y., Qu, H., Smeltzer, C., Li, J., Alvarado, L. M.A., Vrekoussis, M., Richter, A., Wittrock, F., Burrows, J.P., 2017. Enhanced trans-Himalaya pollution transport to the Tibetan Plateau by cut-off low systems. Atmos. Chem. Phys. 17 (4), 3083–3095. https://doi.org/10.5194/acp-17-3083-2017.
Zhang, X., Wang, J., Zhao, J., He, J., Lei, Y., Meng, K., Wei, R., Zhang, X., Zhang, M., Ni, S., Aruffo, E., 2025. Chemical characteristics and sources apportionment of volatile organic compounds in the primary urban area of Shijiazhuang, North China Plain. J. Environ. Sci. 149, 465–475. https://doi.org/10.1016/j.jes.2024.01.009.
Zhang, Z., Zhang, Y., Wang, X., Lü, S., Huang, Z., Huang, X., Yang, W., Wang, Y., Zhang, Q., 2016. Spatiotemporal patterns and source implications of aromatic

hydrocarbons at six rural sites across China's developed coastal regions. J. Geophys. Res. Atmos. 121 (11), 6669–6687. https://doi.org/10.1002/2016JD025115.
Zheng, X., Xie, S., 2025. Differences in the key volatile organic compound species between their emitted and ambient concentrations in ozone formation. Atmos. Chem. Phys. 25 (6), 3807–3820. https://doi.org/10.5194/acp-25-3807-2025.
Zhu, S., Ma, J., Wang, S., Sun, S., Wang, P., Zhang, H., 2023. Shifts of formation regimes and increases of atmospheric oxidation led to ozone increase in North China Plain and Yangtze River Delta from 2016 to 2019. J. Geophys. Res. Atmos. 128 (13), e2022JD038373. https://doi.org/10.1029/2022JD038373.